nature communications

Article

https://doi.org/10.1038/s41467-026-69045-4

Hierarchical design and scalable production of radiative cooling film featuring multispectral camouflage

Received: 1 August 2025

Accepted: 23 January 2026

Published online: 02 February 2026

Check for updates

Yi Jiang[1,2,3,4,5,11], Banghai Wang[1,2,3,4,5,11], Yang An[6,7,8,11], Tianji Liu[6,7,8], Rui Qin[9,10], Dong Zhu[1,2,3,4,5], Min Zhang[6,7,8], Zipeng Chen[1,2,3,4,5], Zhengwei Yang[1,2,3,4,5], Wei Li[6,7,8] ✉, Qiang Li[9,10], Peng Chen[1,2,3,4,5], Yanqing Lu[1,2,3,4,5] ✉, Jia Zhu[1,2,3,4,5] ✉ & Bin Zhu[1,2,3,4,5] ✉

Various outdoor scenarios demand both temperature control and self-protection from environment, which are often contradictory from the optical perspective, thus inspiring many material designs on multispectral camouflage and radiative cooling performance. However, these methods on the basis of one-dimensional photonic crystals or meta-surfaces always rely on stringent fabrication and may result in strong angular dependence. Here, we demonstrate an aluminum-polyamide 66 metal-based polymer bilayer thin film through hierarchical design at both the molecular and microscale levels and scalable production, enabling camouflage in infrared (3-5 μm and 8-14 μm) and laser (10.6 μm) bands with efficient radiative cooling in the non-atmospheric window (5-8 μm and 14-20 μm) while possessing weak angular dependence between −60° to 60°. Furthermore, our films can be tailored with specific emissivity and color to balance camouflage and cooling across diverse environments. This work provides a scalable, low-cost radiative cooling polymer film, advancing practical solutions for multispectral camouflage.

Under various outdoor scenarios, appearance or optical properties of objects (human, animals, facility, etc) often need to serve two major purposes, cooling comfort and self-protection from environment, at the same time. Both of them are crucial in modern society that cooling technology is beneficial amidst the escalating impacts of global warming and rising peak daytime temperatures[1,2] while camouflage provides protection, just as animals disguise themselves against predators[3–7]. However, these two requirements are often contradictory, as they share similar wavebands.

As a typical example, radiative cooling and infrared camouflage both cover mid-infrared band (MIR band, 2.5–20 μm) but require different optical properties. To achieve great cooling performance, radiative cooling materials efficiently emit heat into the outer space (~3 K) through the atmospheric transparency window (3–5 μm and

[1]National Laboratory of Solid State Microstructures, Nanjing University, Nanjing, China. [2]College of Engineering and Applied Sciences, Nanjing University, Nanjing, China. [3]Jiangsu Key Laboratory of Artificial Functional Materials, Nanjing University, Nanjing, China. [4]Frontiers Science Center for Critical Earth Material Cycling, Nanjing University, Nanjing, China. [5]Collaborative Innovation Center of Advanced Microstructures, Nanjing University, Nanjing, China. [6]GPL Photonics Laboratory, Changchun Institute of Optics, Fine Mechanics and Physics, Chinese Academy of Sciences, Changchun, China. [7]Key Laboratory of Luminescence Science and Technology, Changchun Institute of Optics, Fine Mechanics and Physics, Chinese Academy of Sciences, Changchun, China. [8]Chinese Academy of Sciences & State Key Laboratory of Luminescence Science and Applications, Changchun Institute of Optics, Fine Mechanics and Physics, Chinese Academy of Sciences, Changchun, China. [9]State Key Laboratory of Extreme Photonics and Instrumentation, Zhejiang University, Hangzhou, China. [10]College of Optical Science and Engineering, Zhejiang University, Hangzhou, China. [11]These authors contributed equally: Yi Jiang, Banghai Wang, Yang An. ✉e-mail: weili1@ciomp.ac.cn; yqlu@nju.edu.cn; jiazhu@nju.edu.cn; binzhu@nju.edu.cn

8–14 μm) and exchange heat with the ambient (~298 K) through the non-atmospheric transparency window (5–8 μm and 14–20 μm) by infrared thermal radiation. Recently, radiative coolers have been widely used in various fields such as fabric[8], building[9,10], glacier conservation[11], and electronic equipment[12]. For personal thermal management, radiative cooling textiles have gradually moved from research to practical use, with advanced structures including hierarchical fiber membrane[13], bump textured structure[14], particle distributed system[15] and photon-engineered optical device like broadband or selective emitters[16]. However, high infrared radiation in the atmospheric transparency window of materials indicates distinct signal in thermal imagers, which is not beneficial to infrared camouflage. Especially for objects between 30 and 100 °C such as human bodies[17,18], electronic equipment[19], base stations[20], and tent camps[21], they can be easily detected as primary targets due to their elevated temperature and emissivity different from the background, as dictated by Stefan-Boltzmann law. Infrared stealth fabrics have also been studied with several representative strategies like reducing the infrared emissivity or the temperature of the surface. The infrared optical performance regulation often relies on materials like metals, semiconductors and MXenes with broadband low emittance, while surface temperature can be controlled by thermal insulation material like aerogel and hollow structure[22–24]. However, these two methods will both cause thermal discomfort in the human body due to their poor heat dissipation in radiative and conductive capacity, respectively. Therefore, it is essential to develop camouflage materials that not only suppress infrared signatures but also maintain radiative cooling performance in the non-detection window.

With the development of diversified detection technologies combining thermal imagers, laser detectors, and visible telescopes[25,26], it is urgent to realize multispectral compatible camouflage across different bands from various viewing angles. For this purpose, first, the ideal stealth target should have low emittance in the mid-wavelength infrared (MWIR, 3–5 μm) and the long-wavelength infrared (LWIR, 8–14 μm) to minimize thermal radiation contrast with the background in the atmospheric window[24,27–30]. Second, high absorbance at 10.6 μm is required for laser camouflage to interfere with the laser detector receiving a back signal[31,32]. In addition, the color of the stealth object in the visible band (Vis band, 0.38–0.78 μm) should be consistent with that of the background[33,34]. Lastly, it should have high emittance in the non-atmospheric window (5–8 μm and 14–20 μm) for radiative cooling to alleviate thermal issues as clarified above[35–42]. Figure 1a illustrates the ideal spectrum of camouflage from the Vis to MIR band. Such selective spectra have been previously realized through top-down methods such as one-dimensional photonic crystals or metasurfaces[43–47]. These complex optical structures typically not only require stringent top-down fabrication processes with nanometer precision, but also lead to high angular dependence.

Here, through the hierarchically cross-scale design both at the molecular-level and micro-structure, we demonstrate an aluminum-polyamide 66 metal-based polymer bilayer thin film (X-film) by a scalable roll-to-roll electrospinning method that can simultaneously achieve MIR/laser camouflage and radiative cooling well matched with the ideal spectrum. Additionally, it also exhibits weak angular dependence between −60° to 60° in the mid-infrared band due to its randomly stacked structure. A series of samples with different thicknesses in field tests exhibited varying degrees of MIR camouflage while achieving a cooling temperature of 5–10 °C compared with conventional materials with broadband low emittance. Laser camouflage performance is also verified by a simulation experiment. Therefore, this hierarchical X-film with multispectral camouflage and radiative cooling can be well-designed in the face of the varying environmental conditions, providing a scalable, low-cost, and sustainable alternative to the conventional stealth scheme (Supplementary Table 1).

Results

Hierarchical design

The randomly stacked structure always exhibits no optical orientation in a specific direction, thus contributing to uniform color like white or dark in appearance such as nanofiber membranes or porous coatings[48]. It is not only suitable for visible band, but also creates possibilities for an infrared performance scheme with weak angle dependence. However, current materials are usually highly emissive in the mid-infrared band, not satisfying the requirements on multispectral camouflage above. Hence, to achieve low emissivity in MWIR and LWIR with weak angle dependence (Fig. 1b), it is vital to seek elaborate molecular-level design on appropriate material.

Polymers are made up of the basic chain and various functional groups which are the foundation classification of organics (Fig. 1c). Further, functional groups consist of different atoms with diverse bond combinations whose vibration mostly determines the mid-infrared absorption spectrum (Fig. 1d)[13,49]. Thus, we plot the MIR distribution of possible absorption peaks in 18 common organic compounds (alkyl, olefin, alkyne, arene, halohydrocarbon, alcohol, phenol, ether, aldehyde, ketone, carboxylic acid, ester, anhydride, acid halide, amide, nitrile, nitryl and amine) composed of carbon, hydrogen, oxygen, nitrogen and halogen elements (Fig. 1e, Supplementary Table 2 and Supplementary Note 1)[50–54]. To satisfy the requirements of multispectral camouflage in Fig. 1a, the polymer should consist of functional groups that have absorption peaks in the range of 2000–1250 cm^{-1} and 714–500 cm^{-1} (equivalent to 5–8 μm and 14–20 μm) while possess none or weak absorption in the other MIR band (3–5 μm and 8–14 μm) firstly. Therefore, amide and ketone possess the most appropriate functional groups. Alkyl is also taken into account in polymer composition because it acts as the basic element to make up long chains. In summary, the ideal polymer for multispectral camouflage is preferably comprised of alkyl, acylamino, and carbonyl. It is expected that polyamide, also named nylon, meets the requirements above very well[55,56]. The MIR spectrum of polymers is also affected by the absorption peak from crystallization or hydrogen bond interaction in the fabrication process[56–59]. Hence, in simultaneous consideration of laser camouflage at 10.6 μm (~943 cm^{-1}), polyamide 66 (nylon 66 or PA66), which has crystalline peak at 935 cm^{-1} that are more closely to 10.6 μm in comparison with other polyamides like PA6, PA11 and PA12 verified by both references and experimental measurement (Supplementary Fig. 1)[60–62], presents the most desirable absorption band close to the selective MIR spectrum in Fig. 1a.

Fabrication and characterization

With the significant advancement on electrostatic spinning, large-scale films can be produced by a roll-to-roll strategy. Figure 2a shows a flexible meter-scale X-film that exhibits white color and selectively emits infrared light on 5–8 μm and 14–20 μm. Specifically, the absorption property of PA66 and the scattering effect of the plicated aluminum foil substrate jointly contribute to the laser camouflage at 10.6 μm. The fiber diameter of PA66 film was controlled at ~100 nm shown in Fig. 2b so that it would not contribute to the scattering efficiency in the MIR band according to Mie theory, which is further verified by the detailed calculation in Fig. 2c (Supplementary Note 2). Thus, the MIR spectrum of PA66 film is mostly decided by its vibrational absorptions. Note that the FTIR spectrum of PA66 showed its characteristic absorption peak at 1630 cm^{-1} (amide band I), 1534 cm^{-1} (amide band II), 1274 cm^{-1} (amide band III), 935 cm^{-1} (crystalline peak), 685 cm^{-1} (bending vibration of N-H) and 577 cm^{-1} (bending vibration of C=O) (Supplementary Fig. 1), which is consistent with the screening result in Fig. 1e.

Then, we fabricated a series of aluminum-PA66 metal-based polymer bilayer thin films with different thicknesses, named as XN film that N means the thickness of PA66 film. The thickness of the aluminum foil substrate is 25 μm. Figure 2d shows the optical spectrum of

https://doi.org/10.1038/s41467-026-69045-4

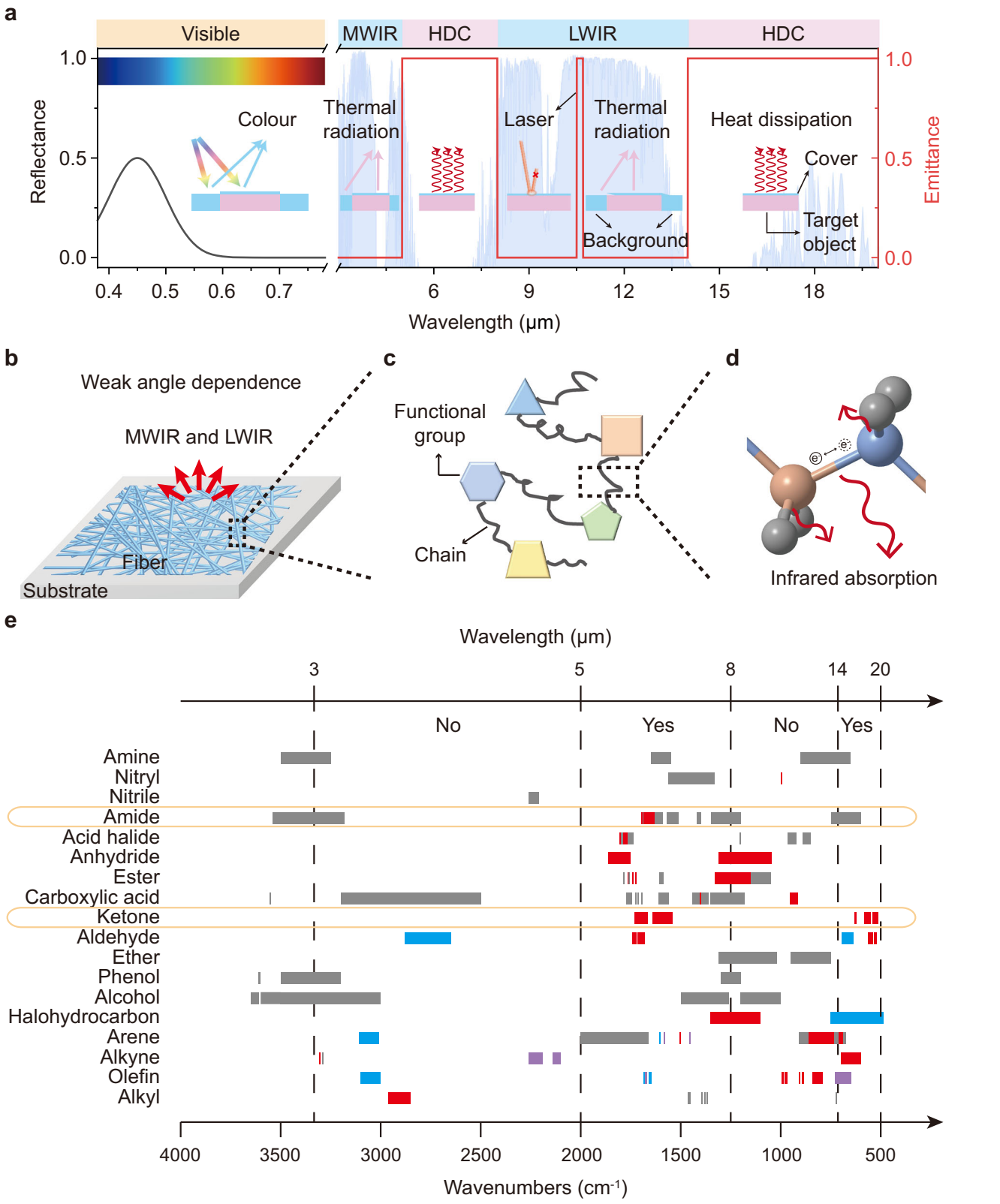

the X-films with varying N, with a low emissivity in MWIR and LWIR, high emissivity outside the atmospheric transparency window, and high absorbance at 10.6 μm, ideal for multispectral camouflage and radiative cooling. The MWIR/LWIR reflection varies from 96.0%/92.5% to 80.7%/59.3% against the thickness of PA66 film from 15 μm to 75 μm, which presents a relationship of gradient descent (Supplementary Fig. 2, Supplementary Note 3 and Supplementary Table 3).

A theoretical model based on the structure of X-films was further constructed to evaluate the angular sensitivity on the spectrum of X-films. It demonstrated that the reflection varied a little when the angle changed from −60° to 60° in both MWIR and LWIR, which indicated the infrared camouflage potential at a broad detection viewing angle range (Fig. 2e and Supplementary Note 4). Then, take X30 for example, we monitored the angle-dependent reflection

https://doi.org/10.1038/s41467-026-69045-4

Fig. 1 | Concept and design for multispectral camouflage. a The ideal spectrum of multispectral camouflage from the visible to mid-infrared band. It includes visible camouflage (color exhibition in 0.38–0.78 μm), mid-infrared camouflage (low emittance in 3–5 μm and 8–14 μm), laser camouflage (high absorbance at 10.6 μm), and heat dissipation channel (HDC, high emittance in 5–8 μm and 14–20 μm for radiative cooling). The blue shade is the atmospheric transmittance spectrum. **b** Schematic of micro-structure of the fibrous membrane. The randomly stacked structure on substrate brings low emissivity in MWIR and LWIR with weak angular dependence. **c** Schematic of polymers with the basic long chain and various functional groups. **d** Schematic of infrared emission by the vibration of chemical bonds. Orange and blue ball, C atom; gray ball, H atom. **e** Mid-infrared distribution of possible absorption peaks in common organic compounds for material screening. The red, blue, purple, and gray shaded areas represent strong, medium, weak, and uncertain absorption strength, respectively. The dotted lines indicate the boundary at 3 μm, 5 μm, 8 μm, 14 μm, and 20 μm, corresponding to 3333 cm^{-1}, 2000 cm^{-1}, 1250 cm^{-1}, 714 cm^{-1}, and 500 cm^{-1}, respectively. "Yes" and "No" mean that the region does or does not need to have absorption peaks according to the ideal spectrum. After screening, the ideal polymer can only be comprised of alkyl, acylamino, and carbonyl, which are circled by a yellow border. In the end, polyamide is identified as the most appropriate material.

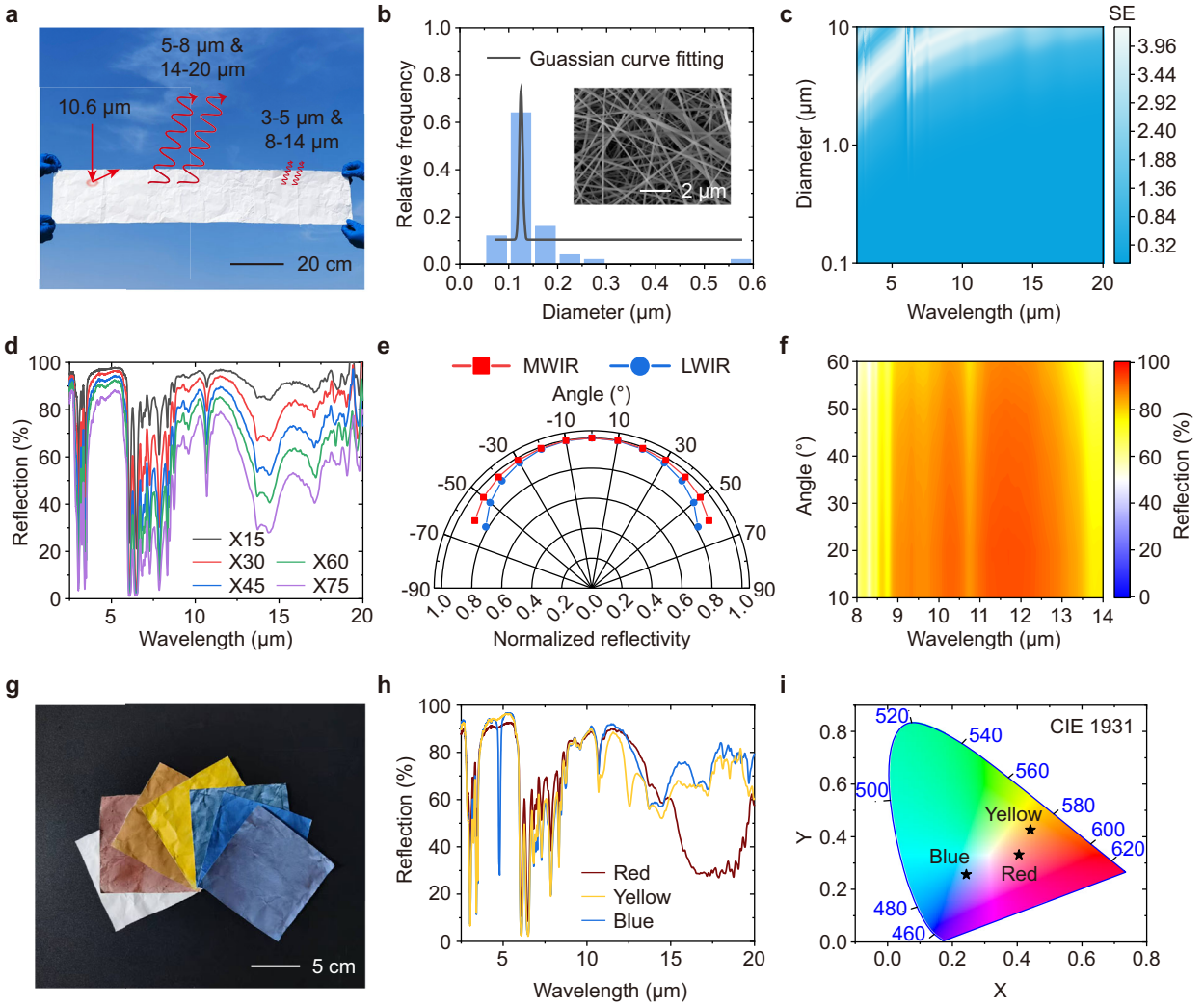

Fig. 2 | Fabrication and characterization of the X-film. a Photograph of a flexible meter-scale X-film. **b** The statistical distribution of the diameters of the PA66 fibers. The inset shows a scanning electron microscopy image of PA66 film. **c** Simulation of the scattering efficiency (SE) of PA66 nanofibers with the diameter from 0.1 to 10 μm in the mid-infrared band. **d** The mid-infrared spectrum of a series of X-films with varying thicknesses of PA66 film. The number after X indicates the thickness of PA66 film whose unit is μm. The thickness of the aluminum substrate is 25 μm. **e** The normalized reflectivity of the simulated model in the MWIR and LWIR against varying angles from −60° to 60°. The angular sizes represent the angles to the normal of the sample surface. **f** Reflection spectra of X30 as a function of angles in the LWIR. It is observed that X-films have weak angular dependence, which is highly desirable in practical applications. **g** The optical photograph of colored X-films. They can exhibit various colors by a mixture of single or two pigments. **h** The mid-infrared spectrum of X-films with three primary colors. The selective optical performance keeps well after adding pigments. **i** The CIE color space plot of X-films with three primary colors.

spectrum in the LWIR. It is found that the positions of absorption peaks (especially in 10.6 μm) and overall reflection intensity are nearly unchanged between 10° to 60° of angles, suggesting that the spectrum of X-films has a weak angular dependence, which is significant for practical applications since the observation angle of infrared camera varies greatly in the processing of moving (Fig. 2f).

Considering visible camouflage, we loaded pigments on the X-films by a scalable spraying process (Supplementary Fig. 3). As shown in Supplementary Fig. 4, the pigments should selectively absorb visible light complementary to the desired color while having no effects on the MIR property of X-films, especially having no absorbance in MWIR and LWIR so that it can achieve infrared, laser, visible

camouflage, and radiative cooling simultaneously. Iron oxide (Fe_2O_3), α-hydroxyl oxidize iron (α-FeOOH), and ferric ferrocyanide ($Fe_4[Fe(CN)_6]_3$) were selected as three primary colors (red, yellow, and blue, respectively) due to their weak absorption in the MWIR and LWIR (Supplementary Fig. 5). The as-prepared films in various colors were exhibited in Fig. 2g, showing white, red, brown, yellow, cyan, blue, and dusty blue from left to right. White is the bottom color of X-films and red, yellow, blue are basic colors by adding a single pigment. Brown, cyan, and dusty blue are secondary colors by mixture of two in the three primary colors. Then, we measured the MIR spectrum (Fig. 2h) and visible spectrum (Supplementary Fig. 6) of X-films with three primary colors. The MIR spectra kept a similar trend with the spectrum in Fig. 2d, maintaining high reflectance in 3–5 μm and 8–14 μm, high emittance in 5–8 μm and 14–20 μm, and high absorbance at 10.6 μm. The visible spectra revealed the dominant reflection peaks around 750 nm, 600 nm, and 450 nm, matching the colors of red, yellow, and blue, respectively, which were further shown in the CIE color space plot (Fig. 2i). The colored X-films gradually darkened as the concentrations of pigments increased, while remaining the selective spectra in the MIR wavelength range and corresponding reflection peaks in the visible wavelength range (Supplementary Figs. 7–9). This spectral property had also been verified effective in X-films with other colors such as brown, cyan, and dusty blue (Supplementary Fig. 10).

Multispectral camouflage, radiative cooling performance and increased durability

The MIR camouflage and radiative cooling effects of the X-films were then evaluated via indoor experiments firstly. A heating sheet connected with X-films by thermal compounds was designed as an experimental setup, which is insulated from heat conduction by foam. X-films with different thicknesses of PA66 (X30, X45, X62, X72), an aluminum foil (X0), and a case without any covering (bare) were used as controls (Fig. 3a and Supplementary Fig. 11) while the initial temperature of heating sheets before covering is set as 55 °C. The infrared photographs in LWIR indicated that compared with the bare control, all X-films exhibited different potentials of camouflage performance (Fig. 3b). The stealth effect became better with the thinning of PA66 film and the aluminum foil showed the most complete camouflage due to its low-emissivity. The same trend was also demonstrated in MWIR photographs (Fig. 3c). However, the MIR property of aluminum foil is broadband low emissive so that it possessed a temperature increase of 15 °C in comparison with initial state when covered on the heating sheet, which may cause thermal problems or extra cooling energy consumption (Supplementary Fig. 12 and Fig. 3d). X-films are expected to alleviate this phenomenon because they had a cooling temperature of 5–10 °C compared to X0. Contrary to the relation between camouflage performance and the thickness of PA66 film, the heat dissipation capacity of X-films was correlated positively with the thickness of PA66 film, where it existed a balance. Thus, in situations where stealth is not as demanding, various X-films can be selected to meet the basic requirements on camouflage and further enlarge cooling performance. Then, a heating power test was also conducted to demonstrate the MIR property of different controls (Fig. 3e). To maintain the temperature of the heating sheet at 55 °C, the bare control demanded the heating power up to 428 W m^{-2} due to its high MIR emissivity while the case covered with X0 film required the lowest (272 W m^{-2}). The controls with X-films fell in between (316 W m^{-2}, 336 W m^{-2}, 362 W m^{-2}, and 374 W m^{-2} for X30, X45, X60, and X72, respectively) by virtue of their great radiative cooling performance in the non-atmospheric window. Thus, both the temperature test and heating power test verify that X-films can achieve MIR camouflage and radiative cooling effects, which are corresponding to the optical spectra above.

We also evaluated the camouflage and cooling performance using the same device outdoors at night. It could focus more on the MIR spectrum because there was no sunlight to bring the extra energy input. In comparison with indoors, convection was also taken into consideration to reflect the actual situation outdoors. Similarly, all the X-films exhibited good stealth effects and the trend with the thickness of PA66 film was consistent with the indoor test (Supplementary Fig. 13). In the temperature test, the cases with X30, X45, X62, and X72 film were 5 °C, 9 °C, 10 °C, and 12 °C cooler than the case with X0 film, respectively, showing good cooling capacity as well (Supplementary Fig. 14). Then, we further assessed the temperature control of X-films under solar exposure. The nylon fiber can scatter solar radiation by Mie theory, thus exhibiting high reflectivity in solar band (Supplementary Fig. 15). During the field temperature test in the daytime, the cases with X45 and X72 films were 7 °C and 11 °C cooler than the case with X0 film, maintaining superior cooling performance. All the results consistently demonstrate the splendid properties of X-films, further illustrating the importance of material selection on PA66.

To demonstrate the weak angular dependence of X-films, infrared photographs in different observation angles between 10° to 60° were captured. An X30 sample with the dimension of 3 cm * 3 cm is tightly connected with a heater whose temperature is ~75 °C. We ensured the precise observation angles by holding the infrared camera still and rotating the heating sheet to the corresponding angles. It is found that the colors of the sample remain nearly unchanged between 10° to 60°, suggesting that the X-films have weak angular dependence and exhibit great camouflage performance in varying observation angles (Fig. 3f).

Having verified the infrared camouflage and radiative cooling capacity of X-films, it is important to evaluate the other requirements such as laser camouflage. We designed an indoor simulated experiment against the outdoor test to demonstrate the laser camouflage effect that less back signal received means better laser camouflage. As shown in Fig. 3g, a quantum cascade laser was used to emit light at 10.6 μm and the strength of the back signal was recorded by an optical power meter. Samples with PA66 spun on the smooth aluminum plates and on the plicated aluminum foils were used to clarify the influences on laser camouflage by the absorbance of the PA66 layer and the Geometric scattering effect of substrates at 10.6 μm, respectively (Supplementary Fig. 16). As shown by optical path transmission schematic in Supplementary Figs. 17 and 18, the sample with absorption or scattering effect both can weaken the received signal strength in the optical power meter. The detailed results illustrated that the reflection strength of the back signal of X-films with different thicknesses of PA66 films on the plicated aluminum foils decreased rapidly compared to bare aluminum foils under the combined action of absorption and scattering, which all exhibited good laser camouflage potential (Fig. 3h).

Durability is also an important problem in practical applications. X-films have good mechanical properties under mechanical stress (Supplementary Figs. 19 and 20). For further optimization, we increased the stability of X-films by polyethylene (PE) film encapsulation on the surface, named as XNP film (N means the thickness of PA66 film). Figure 3i demonstrated that the curve shapes of MIR spectra were similar between XNP film and XN film because polyethylene showed high mid-infrared transmission which has only C-C and C-H bonds. Then, a series of tests were conducted to verify the environmental durability, including low-temperature tests, high-temperature tests, acid tests, alkali tests, water flushing tests, UV exposure tests, and wind tests. The mass changes were less than 1.0% after each of these seven tests, indicating the films were well preserved (Fig. 3j). Additionally, the reflection in LWIR also remained nearly unchanged so that the MIR property of XNP films would work for a long time (Fig. 3k and Supplementary Fig. 21). The scratch and abrasion resistance test also verified that the XNP film possessed good durability (Supplementary Figs. 22 and 23). These satisfactory results all illustrate that the durability of XNP films has been increased, which is expected to stand up to practical use.

https://doi.org/10.1038/s41467-026-69045-4

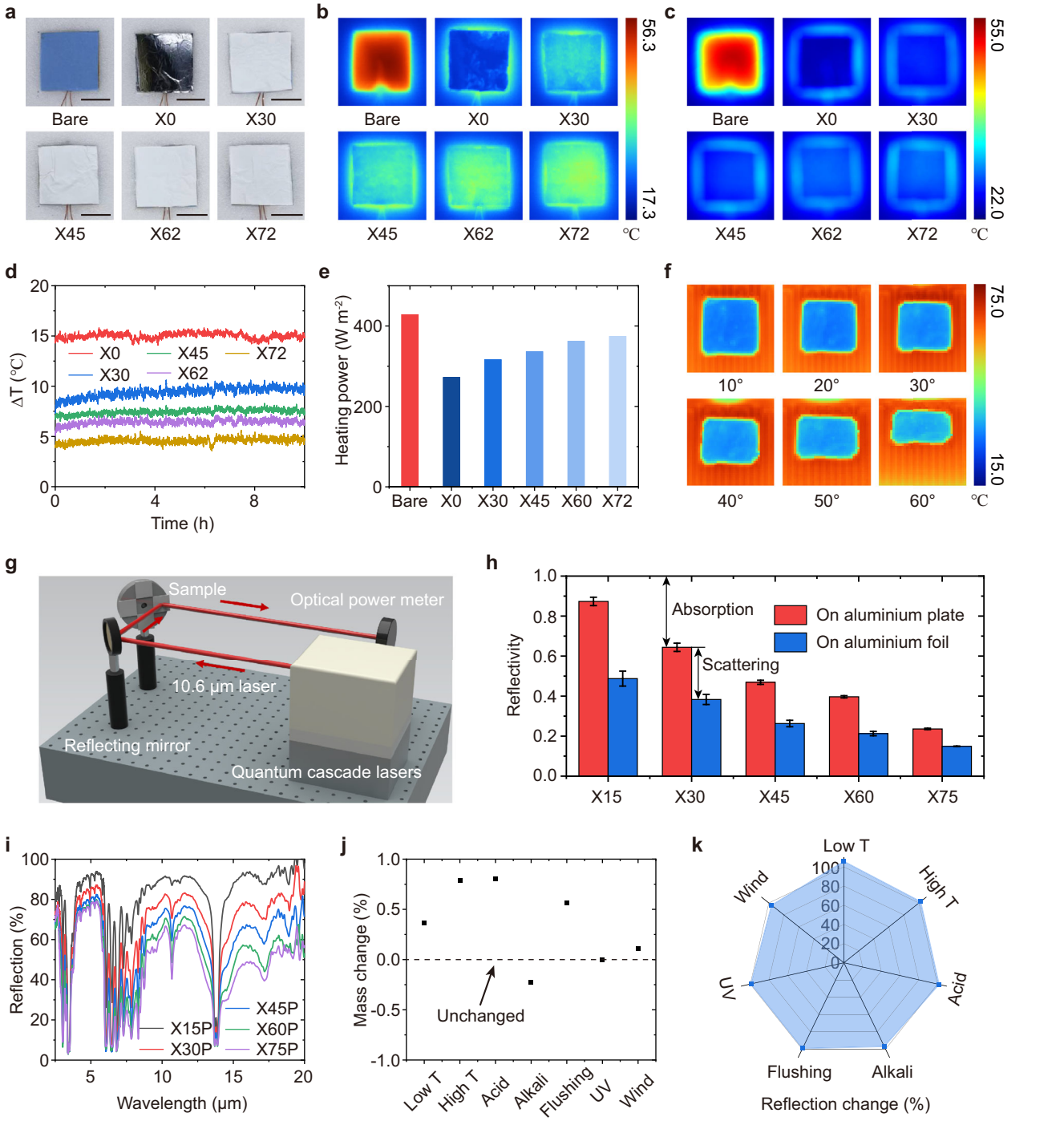

Fig. 3 | Multispectral camouflage and radiative cooling performance of the X-films. a Optical photographs of different control groups. The controls contain the cases with no covering (bare), aluminum foil (X0), and X-films (X30, X45, X62, X72). The sizes of the heater and samples are 10 cm * 10 cm. Scale bar: 5 cm. **b**, **c** Infrared photographs in LWIR and MWIR, respectively. The camouflage performance of X-films will be enhanced with the thinning of PA66 film. **d** The temperature difference between bare control and the cases with X0 and X-films. **e** Comparison of the heating power recorded on different controls when keeping the temperature of the heating sheet at 55 °C. X-films have better radiative cooling performance than aluminum foil. **f** Infrared photographs captured at varying observation angles between 10° to 60°. It verifies that the X-films have weak angular dependence. **g** Schematic of the indoor simulated experiment to verify the laser camouflage performance at 10.6 μm. The light at the wavelength of 10.6 μm is emitted by a quantum cascade laser and the back signal is received by an optical power meter. **h** The reflectance in 10.6 μm of X-films with different thicknesses of PA66 films on the smooth aluminum plates and on the plicated aluminum foils. The data is presented as the mean ± s.d. ($n = 3$). It illustrates that the laser camouflage potential of X-films is not only attributed to the absorbance of PA66 at 10.6 μm but also the Geometric scattering effect caused by the plicated and flexible aluminum foil substrate. **i** The mid-infrared spectrum of XNP films. The curve shape remains similar after polyethylene film encapsulation on the X-films. **j** The mass change of XNP films undergoing durability test. **k** The reflection change in 8–14 μm of XNP films undergoing durability test. They have nearly no change in both mass and LWIR reflection, indicating its satisfactory environmental durability.

Well-designed camouflage

It is common to carry electronic equipment like batteries or communication devices on a few-day journey. Thus, when encountering unexpected surveillance in the field, timely camouflage against visible and infrared detection is necessary due to the vivid color differences in optical photographs and the temperature-induced contrasts (~37 °C for human body and more than 70 °C for electronic equipment while 20 °C for environment) in infrared image in comparison with background. Meanwhile, efficient radiative cooling performance is beneficial to humans on long-term standby and devices in prolonged operation, which is mainly focused on non-atmospheric window (5–8 μm and 14–20 μm) when satisfying infrared camouflage. Additionally, it is necessary to decrease the back signal strength at 10.6 μm for laser camouflage.

Then, cotton woven fabrics attached by X-films (X-fabric) and aluminum films (Al-fabric) were worn on dummies with heating sheets on the main parts such as chest and abdomen for temperature regulation as a comparison to clarify the multispectral camouflage and cooling performance. The X-fabric not only exhibited infrared camouflage effect similar with the Al-fabric (Fig. 4a) but also owned a better visible camouflage than the Al-fabric (Fig. 4b). Meanwhile, the temperatures of chest and abdomen under the X-fabric were both lower than those under the Al-fabric due to its extra radiative heat dissipation capacity in the non-atmospheric window (Fig. 4c). The laser camouflage potential was evaluated via the detected temperature of the bright spot which was caused by the emitted light at 10.6 μm of a quantum cascade laser in the captured infrared images. Higher temperatures meant higher echoed signals, further representing lower absorptive ability and worse laser camouflage of samples. As shown in Fig. 4d, the X-fabric had a lower temperature than the Al-fabric at the same power, indicating a better laser camouflage effect. Also, the laser signal on the X-fabric disappeared in the background as the emitter power decreased from 0.1 P to 0.018 P (P stands for the original laser power) while that of the Al-fabric not, which implied that the X-fabric could suffer shorter maximum detection distance in actual use. Then, infrared images were taken from −60° to 60° at a distance of ~2 m (Fig. 4e). It was verified that the X-fabric had good infrared camouflage performance from various angles and maintained a consistent color due to its weak angular dependence, which was beneficial to flexibly cope with mobile detectors in practical applications.

The X-fabric was also well-designed by body region with different color and emissivity against various actual scenarios like shrubberies. Figure 4f presented the infrared and optical images of a human wearing garments made of three different textiles on a cloudy day. The images showed that although the green cotton fabric exhibited a similar color to the shrubberies in comparison with the white cotton fabric, it still could not achieve infrared camouflage due to its high emissivity as the same as the white cotton fabric. However, the regionalized well-designed green X-fabric displayed a similar color to the background in both infrared and optical photographs.

Additionally, the requirements on multispectral camouflage are changing for integrating into the various environmental backgrounds (Supplementary Figs. 24, 25 and Supplementary Note 5). Thus, the X-films can be well-designed by adjusting the thickness of PA66 film, the mass ratio of loaded pigments, and the selection of PE film to achieve appropriate reflectivity or emissivity for better integrating into environments (Supplementary Fig. 26 and Supplementary Note 6). The recommended thickness range of PA66 film balancing camouflage and cooling performance is from 30 μm to 75 μm. As an example, the devised brown X-film showed a similar color to sand and it could provide good infrared camouflage for electronic equipment like a fully operational mobile phone (Supplementary Fig. 27). Furthermore, the surface treatment of substrate is also beneficial for X-films to achieve better infrared camouflage performance against various surroundings[63].

Discussion

In summary, we have proposed an aluminum-PA66 metal-based polymer bilayer thin film through hierarchical design appropriate for multispectral camouflage in infrared (3–5 μm and 8–14 μm) and laser (10.6 μm) bands with efficient radiative cooling performance (5–8 μm and 14–20 μm). It features a verified weak angular dependence between −60° to 60° in the LWIR. These properties of camouflage and cooling have been proven effective through a series of X-films with various thicknesses in subsequent practical tests. Therefore, X-films can be well-designed for multispectral camouflage and cooling performance to adapt to different environments such as white walls, shrubberies, and sands. In addition, it also demonstrates a functional group screening method for polymer-based complex spectral design, which opens up tremendous opportunities for polymer based photonic devices.

Methods

Fabrication of the X-films

PA66 (Rhawn, M_w = 679) was dissolved in formic acid/acetic acid with a temperature of 40 °C and magnetic stirring at 500 rpm until it formed a clear solution. The ratio of solute and solvent is 1 g PA66: 2.5 ml formic acid: 2.5 ml acetic acid. The as-prepared solution was electrospun at a tip-to-collector distance of 15 cm, a voltage difference of 25.5 kV, and a flow rate of 0.1 ml h^{-1} with 18-gauge needle tips. A drum wrapped with a layer of aluminum film was used for collecting the PA66 nanofibers. The rotation speed of the collector was 80 rpm. All electrospinning experiments were conducted at a room temperature of 20 °C and a relative humidity of ~40%. The thickness of X-films was measured with a micrometer caliper which was mainly determined by spinning time. The XNP films were fabricated by XN films hot pressed with PE film (~30 μm) at 110 °C.

Fabrication of the colored X-films

The pigments (Iron oxide (Aladdin, 99.5% metals basis), α-hydroxyl oxidize iron (Sigma-Aldrich, 30–63% Fe), ferric ferrocyanide (Aladdin, biological stain)) for corresponding colors (a mixture of one or more pigments) were dispersed in ethanol by magnetic stirring and ultrasonic cleaning. The X30 films were selected as the spraying substrate. The as-prepared solution was sprayed onto the pre-heated X30 films by a spray gun (SATHN, W-71). The depth of color was determined by the mass loading of pigments that could be adjusted through spray time and spray speed. The initial mass of the X30 film was recorded as m_1 and the final mass of the colored X30 film after evaporating ethanol was recorded as m_2. The mass ratio of the loaded pigments ω_{color} was calculated by $(m_2-m_1)/m_2$.

Material characterizations

The microscopic image of PA66 nanofibers was captured by scanning electron microscopy (SEM; TESCAN, MIRA3). The FTIR spectrum was measured by Nicolet IS10. The mid-infrared spectrum (2.5–20 μm) was measured using a Fourier transform infrared spectrophotometer (Thermo Fisher Scientific, Nicolet IS50R) loaded with an integrating sphere (Pike, 4P-GPS-020-SL). The angle-dependent mid-infrared spectrum was measured by the Fourier transform infrared spectrophotometer (VERTEX 80 v, Bruker) coupled with a thermal emission collection setup while keeping different tilt angles of the tested sample. The solar spectrum (0.3–2.5 μm) was measured by an ultraviolet-visible spectroscopy (SHIMADZU, UV3600) equipped with an integrating sphere (ISR-310). The infrared photographs in 8–14 μm were captured by an LWIR camera (Fluke, TiX580). The infrared photographs in 3–5 μm were captured by a MWIR camera (Telops, FAST M200).

https://doi.org/10.1038/s41467-026-69045-4

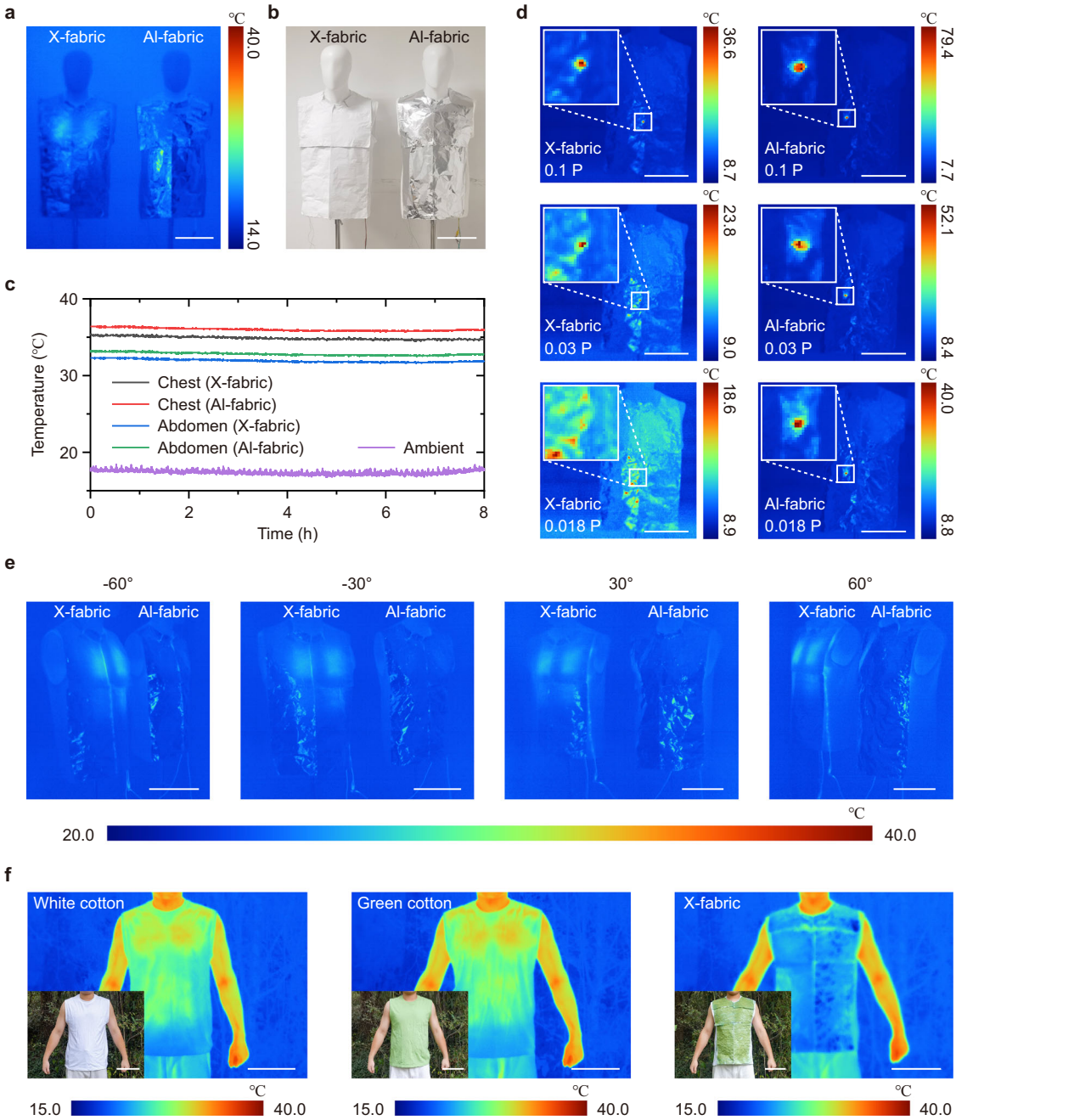

Fig. 4 | Well-designed camouflage for various environments. a, **b** The infrared and optical photographs of the X-fabric and Al-fabric worn on dummies. The X-fabric can exhibit similar infrared camouflage to the Al-fabric but better visible camouflage than that. Scale bar: 20 cm. **c** The temperatures of chest and abdomen under the X-fabric and Al-fabric. **d** The infrared photographs of the X-fabric and Al-fabric under different laser powers. The bright spots at different temperatures are caused by the reflected signal that the quantum cascade laser at 10.6 μm hits on the fabrics when adding varying attenuators. A higher temperature means worse laser camouflage potential. The illustrations show enlarged images of these bright spots. 0.1 P, 0.03 P, and 0.018 P represent the laser power is attenuated to 0.1, 0.03, 0.018 times of the original, respectively. Scale bar: 20 cm. **e** Infrared photographs of the X-fabric and Al-fabric worn on dummies at the observation angles of −60°, −30°, 30°, and 60°, respectively. It is verified that the X-fabric exhibits infrared camouflage performance similar to the Al-fabric from various detection angles and maintains the color consistent due to its weak angular dependence. Scale bar: 20 cm. **f** Infrared and optical photographs of a human wearing vests consisting of white cotton fabric, green cotton fabric, and the regionalized well-designed green X-fabric. The X-fabric can achieve both visible and infrared camouflage against the background of shrubberies. Scale bar: 20 cm.

Measurement of radiative cooling performance and infrared camouflage performance

The temperature was monitored by K-type thermocouples and real-time recorded by a recorder (Asmik, MIK R6000C). A Kapton heater sheet was used as an internal heat source with a size of 10 cm × 10 cm. The initial temperatures of heating sheets before covering were set as 55 °C in all control groups with a heating power of ~5.2 W. The heating power test was conducted with a temperature feedback circuit. The temperature of the tested sample was controlled at 55 °C by heating. Through the temperature controller and power meter (Chroma, 66205), the heating power of the sample could be achieved, which was equivalent to radiative cooling performance. The outdoor temperature was monitored through the same method used in the indoor test as mentioned above. All the temperature tests, power tests, and LWIR

image captures were conducted in Nanjing (32.12° N, 188.96° E) while the MWIR image capture was conducted in Zhejiang (30.26° N, 120.12° E).

Measurement of laser camouflage performance

A quantum cascade laser (Block Engineering, LaserTune) was controlled to emit 10.6 μm light and an optical power meter (MKS Ophir 3 A) was used to record the strength of the back signal. The power of the back signal with the aluminum plate or foil was recorded as P_r. The power of the back signal with samples was recorded as P_s. The reflection strength of the back signal was calculated by P_s/P_r.

Environmental durability tests

(1) Low-temperature test: the samples were put in a freezer with a constant temperature of −40 °C for 1 week. (2) High-temperature test: the samples were put on a heating stage with a constant temperature of 80 °C for 1 week. (3) Acid test: the samples were immersed in sealed hydrochloric acid aqueous solution with pH = 4 for 1 week. (4) Alkali test: the samples were immersed in a sealed potassium hydroxide aqueous solution with pH = 10 for 1 week. (5) Water flushing test: the samples were fixed with a tilt angle of ~45° from the water faucet with a water flow rate of 50 ml s^{-1}. The water flowed over the samples into the pool. The flushing process was 10 min. (6) UV exposure test: the samples were illuminated by a UV lamp (6 W) in a closed chamber for 1 week. (7) Wind test: the samples were fixed on a glass in front of the fan with the gas flow of 83 cubic feet per minute (CFM) for 1 h. The mass changes and spectral changes before and after the experiments above were recorded to evaluate the durability of the samples. (8) Scratch resistance test: sharpened pencils with different hardness levels were pushed on the sample's surface to create a scratch over 1 cm in length at a 45° angle. The test was conducted until a pencil ruptured the coating, which meant the hardest pencil that did not cause rupture was recorded as the hardness level of the coating. The load weight was 500 g during the test. (9) Abrasion resistance test: a glass with the sample attached was placed upside down on the sandpaper (grit size 400). A 100 g weight was placed on the surface of the glass. The glass was moved around a 10 cm square as one cycle (from position 1 to 2 to 3 to 4 and then back to position 1). The infrared spectra and visual appearance were recorded before and after the test.

On-body camouflage effects

A volunteer wore three different textiles in front of the shrubberies, which are white cotton fabric, green cotton fabric and cotton wove fabric attached by green X-films, respectively. The optical photographs and infrared images were captured to evaluate the visible and infrared camouflage performance. Written and informed consent was received from all volunteers.

Data availability

All data are available in the main text or the Supplementary Information and can be available from the corresponding author upon request. Source data are provided with this paper.

References

1. Raman, A. P., Anoma, M. A., Zhu, L., Rephaeli, E. & Fan, S. Passive radiative cooling below ambient air temperature under direct sunlight. *Nature* **515**, 540–544 (2014).
2. Fan, S. & Li, W. Photonics and thermodynamics concepts in radiative cooling. *Nat. Photonics* **16**, 182–190 (2022).
3. Stevens, M. & Merilaita, S. Animal camouflage: current issues and new perspectives. *Philos. Trans. R. Soc. B* **364**, 423–427 (2009).
4. Stevens, M. & Ruxton, G. D. The key role of behaviour in animal camouflage. *Biol. Rev.* **94**, 116–134 (2019).
5. Teyssier, J., Saenko, S. V., van der Marel, D. & Milinkovitch, M. C. Photonic crystals cause active colour change in chameleons. *Nat. Commun.* **6**, 6368 (2015).
6. Xu, C., Stiubianu, G. T. & Gorodetsky, A. A. Adaptive infrared-reflecting systems inspired by cephalopods. *Science* **359**, 1495–1500 (2018).
7. Cuthill, I. Camouflage. *J. Zool.* **308**, 75–92 (2019).
8. Wu, R. et al. Spectrally engineered textile for radiative cooling against urban heat islands. *Science* **384**, 1203–1212 (2024).
9. Lin, K. et al. Hierarchically structured passive radiative cooling ceramic with high solar reflectivity. *Science* **382**, 691–697 (2023).
10. Zhao, X. et al. A solution-processed radiative cooling glass. *Science* **382**, 684–691 (2023).
11. Cao, N. N. et al. Challenges to materials for local glacier conservation. *Nat. Water* **3**, 251–255 (2025).
12. Zhang, J. H. et al. Versatile self-assembled electrospun micropyramid arrays for high-performance on-skin devices with minimal sensory interference. *Nat. Commun.* **13**, 5839 (2022).
13. Li, D. et al. Scalable and hierarchically designed polymer film as a selective thermal emitter for high-performance all-day radiative cooling. *Nat. Nanotechnol.* **16**, 153–158 (2021).
14. Ding, Z. et al. Iridescent daytime radiative cooling with no absorption peaks in the visible range. *Small* **18**, 2202400 (2022).
15. Zeng, S. et al. Hierarchical-morphology metafabric for scalable passive daytime radiative cooling. *Science* **373**, 692–696 (2021).
16. Wu, X. et al. A dual-selective thermal emitter with enhanced subambient radiative cooling performance. *Nat. Commun.* **15**, 815 (2024).
17. Hu, R. et al. Emerging materials and strategies for personal thermal management. *Adv. Energy Mater.* **10**, 1903921 (2020).
18. Du, X., Li, J., Zhu, B. & Zhu, J. Designing hierarchical structures for innovative cooling textile. *Nano Res.* **17**, 9202–9224 (2024).
19. Shi, Y. et al. A novel multi-dimensional structure of graphene-decorated composite foam for excellent stealth performance in microwave and infrared frequency bands. *J. Mater. Chem. A* **10**, 7705–7717 (2022).
20. Tu, R., Liu, X.-H., Li, Z. & Jiang, Y. Energy performance analysis on telecommunication base station. *Energy Build.* **43**, 315–325 (2011).
21. Zhang, L., Meng, X., Liu, F., Xu, L. & Long, E. Effect of retro-reflective materials on temperature environment in tents. *Case Stud. Therm. Eng.* **9**, 122–127 (2017).
22. Zhang, Y. et al. A waste textiles-based multilayer composite fabric with superior electromagnetic shielding, infrared stealth and flame retardance for military applications. *Chem. Eng. J.* **471**, 144679 (2023).
23. Ma, H. et al. Double-sided functional infrared camouflage flexible composite fabric for thermal management. *Ceram. Int.* **49**, 16422–16432 (2023).
24. Cui, G. et al. Freestanding graphene fabric film for flexible infrared camouflage. *Adv. Sci.* **9**, 2105004 (2022).
25. Gade, R. & Moeslund, T. B. Thermal cameras and applications: a survey. *Mach. Vis. Appl.* **25**, 245–262 (2014).
26. Kaushal, H. & Kaddoum, G. Applications of lasers for tactical military operations. *IEEE Access* **5**, 20736–20753 (2017).
27. Chandra, S., Franklin, D., Cozart, J., Safaei, A. & Chanda, D. Adaptive multispectral infrared camouflage. *ACS Photonics* **5**, 4513–4519 (2018).
28. Fang, S. et al. Self-assembled skin-like metamaterials for dual-band camouflage. *Sci. Adv.* **10**, eadl1896 (2024).
29. Lin, Z. et al. Flexible meta-tape with wide gamut, low lightness and low infrared emissivity for visible-infrared camouflage. *Adv. Mater.* **11**, 2410336 (2024).
30. Woo, H. K. et al. Visibly transparent and infrared reflective coatings for personal thermal management and thermal camouflage. *Adv. Funct. Mater.* **32**, 2201432 (2022).

31. Kang, Q., Li, D., Wang, W., Guo, K. & Guo, Z. Multiband tunable thermal camouflage compatible with laser camouflage based on GST plasmonic metamaterial. *J. Phys. D Appl. Phys.* **55**, 065103 (2021).
32. Huang, J. et al. Large-area and flexible plasmonic metasurface for laser-infrared compatible camouflage. *Laser Photon. Rev.* **17**, 2200616 (2023).
33. Kim, J., Park, C. & Hahn, J. W. Metal-semiconductor-metal metasurface for multiband infrared stealth technology using camouflage color pattern in visible range. *Adv. Opt. Mater.* **10**, 2101930 (2022).
34. Pikul, J. H. et al. Stretchable surfaces with programmable 3D texture morphing for synthetic camouflaging skins. *Science* **358**, 210–214 (2017).
35. Zhu, H. et al. High-temperature infrared camouflage with efficient thermal management. *Light Sci. Appl.* **9**, 60 (2020).
36. Pan, M. et al. Multi-band middle-infrared-compatible camouflage with thermal management via simple photonic structures. *Nano Energy* **69**, 104449 (2020).
37. Lim, J. S. et al. Multiresonant selective emitter with enhanced thermal management for infrared camouflage. *ACS Appl. Mater. Interfaces* **16**, 15416–15425 (2024).
38. Huang, L. et al. Multiband camouflage design with thermal management. *Photonics Res.* **11**, 839–851 (2023).
39. Kang, Q., Guo, K. & Guo, Z. A tunable infrared emitter based on phase-changing material GST for visible-infrared compatible camouflage with thermal management. *Phys. Chem. Chem. Phys.* **25**, 27668–27676 (2023).
40. Zhou, P. et al. Visible-infrared camouflage with efficient thermal management based on surface morphology regulation. *Opt. Laser Technol.* **176**, 110985 (2024).
41. Xi, W. et al. Ultrahigh-efficient material informatics inverse design of thermal metamaterials for visible-infrared-compatible camouflage. *Nat. Commun.* **14**, 4694 (2023).
42. Qin, B., Zhu, Y., Zhou, Y., Qiu, M. & Li, Q. Whole-infrared-band camouflage with dual-band radiative heat dissipation. *Light Sci. Appl.* **12**, 246 (2023).
43. Zhu, H. et al. Multispectral camouflage for infrared, visible, lasers and microwave with radiative cooling. *Nat. Commun.* **12**, 1805 (2021).
44. Jiang, X. et al. Implementing of infrared camouflage with thermal management based on inverse design and hierarchical metamaterial. *Nanophotonics* **12**, 1891–1902 (2023).
45. Li, X. et al. Multispectral camouflage nanostructure design based on a particle swarm optimization algorithm for color camouflage, infrared camouflage, laser stealth, and heat dissipation. *Opt. Express* **31**, 44811–44822 (2023).
46. Luo, M. et al. Tunable infrared detection, radiative cooling and infrared-laser compatible camouflage based on a multifunctional nanostructure with phase-change material. *Nanomaterials* **12**, 2261 (2022).
47. Feng, X. et al. Large-area low-cost multiscale-hierarchical metasurfaces for multispectral compatible camouflage of dual-band lasers, infrared and microwave. *Adv. Funct. Mater.* **32**, 2205547 (2022).
48. Zhu, B. et al. Subambient daytime radiative cooling textile based on nanoprocessed silk. *Nat. Nanotechnol.* **16**, 1342–1348 (2021).
49. Aili, A. et al. Selection of polymers with functional groups for daytime radiative cooling. *Mater. Today Phys.* **10**, 100127 (2019).
50. Griffiths, P. R. Fourier transform infrared spectrometry. *Science* **222**, 297–302 (1983).
51. Shimanouchi, T. *Tables of Molecular Vibrational Frequencies*, Vol. 1 (National Bureau of Standards, 1972).
52. Socrates, G. *Infrared and Raman Characteristic Group Frequencies: Tables and Charts* (John Wiley & Sons, 2004).
53. Bruice, P. Y. *Organic Chemistry* (Pearson, 2017).
54. Khan, S. A. et al. Fourier transform infrared spectroscopy: fundamentals and application in functional groups and nanomaterials characterization. In *Handbook of Materials Characterization*, (ed Sharma, S.) 317–344 (Cham: Springer International Publishing, 2018).
55. Tong, J. K. et al. Infrared-transparent visible-opaque fabrics for wearable personal thermal management. *ACS Photonics* **2**, 769–778 (2015).
56. Chen, Z. et al. An infrared-transparent textile with high drawing processed Nylon 6 nanofibers. *Nat. Commun.* **16**, 2009 (2025).
57. Holmes, D., Bunn, C. & Smith, D. The crystal structure of polycaproamide: nylon 6. *J. Polym. Sci.* **17**, 159–177 (1955).
58. Seguela, R. Overview and critical survey of polyamide6 structural habits: misconceptions and controversies. *J. Polym. Sci.* **58**, 2971–3003 (2020).
59. Ma, Y., Zhou, T., Su, G., Li, Y. & Zhang, A. Understanding the crystallization behavior of polyamide 6/polyamide 66 alloys from the perspective of hydrogen bonds: projection moving-window 2D correlation FTIR spectroscopy and the enthalpy. *RSC Adv.* **6**, 87405–87415 (2016).
60. Zhang, G., Li, Y. & Yan, D. Polymorphism in nylon-11/montmorillonite nanocomposite. *J. Polym. Sci. Pt. B Polym. Phys.* **42**, 253–259 (2004).
61. Ma, N. et al. Crystal transition and thermal behavior of Nylon 12. *e-Polymers* **20**, 346–352 (2020).
62. Vasanthan, N. & Salem, D. Infrared spectroscopic characterization of oriented polyamide 66: band assignment and crystallinity measurement. *J. Polym. Sci. Pt. B Polym. Phys.* **38**, 516–524 (2000).
63. Huang, Y. et al. Infrared camouflage utilizing ultrathin flexible large-scale high-temperature-tolerant Lambertian surfaces. *Laser Photonics Rev.* **15**, 2000391 (2021).

Acknowledgements

We acknowledge the micro-fabrication center of the National Laboratory of Solid State Microstructures (NLSSM) for technical support. J.Z. acknowledges the support from the XPLORER PRIZE. W.L. acknowledges the support from the New Cornerstone Science Foundation through the XPLORER PRIZE. This work was jointly supported by the National Key Research and Development Programme of China (2022YFA1404704 and 2020YFA0406104), National Natural Science Foundation of China (52372197, 51925204, 52002168, T2525033, 62134009, 62121005), Natural Science Foundation of Jiangsu Province (BK20231540 and BK20243009), Excellent Research Programme of Nanjing University (ZYJH005), research foundation of Frontiers Science Center for Critical Earth Material Cycling (14380214), the Fundamental Research Funds for the Central Universities (021314380184, 021314380208, 021314380190, 021314380140 and 021314380150), and State Key Laboratory of New Textile Materials and Advanced Processing Technologies (Wuhan Textile University, No. FZ2022011).

Author contributions

Y.J., B.Z., and J.Z. conceived the idea. B.Z., W.L., Q.L., P.C., Y.L., and J.Z. supervised the project. Y.J., B.W., Y.A., T.L., R.Q., D.Z., M.Z., Z.C., and Z.Y. designed and carried out all the experiments. Y.J. and T.L. performed the optical modeling. All authors discussed the results and approved the final version of the manuscript.

Competing interests

The authors declare no competing interests.

Additional information

Supplementary information The online version contains supplementary material available at https://doi.org/10.1038/s41467-026-69045-4.

Correspondence and requests for materials should be addressed to Wei Li, Yanqing Lu, Jia Zhu or Bin Zhu.

Peer review information *Nature Communications* thanks Qilong Cheng, Chi Yan TSO, and the other, anonymous, reviewer(s) for their contribution to the peer review of this work. A peer review file is available.